Earth Planets Space, **56**, 859–871, 2004

Exploitation of high-sampling Hi-net data to study seismic energy scaling: The aftershocks of the 2000 Western Tottori, Japan, earthquake

Satoshi Ide[1], Makoto Matsubara[2], and Kazushige Obara[2]

[1]*Department of Earth and Planetary Science, University of Tokyo, Japan*
[2]*National Research Institute for Earth Science and Disaster Prevention, Japan*

(Received February 2, 2004; Revised June 15, 2004; Accepted July 26, 2004)

High-quality seismic data with broad frequency band are essential for the study of seismic energy, E_s, and its scaling with seismic moment, M_o. The 2000 Western Tottori earthquake (M_w 6.6) and its aftershocks as recorded by NIED Hi-net including undistributed high-sampling data provide an excellent data set for this purpose. In this study we use: 1) regular data sampled at 100 sps of small and intermediate (M 2–4) aftershocks just after the mainshock, and, 2) 100 sps data and high sampling 1000 sps data of small events (M 0–3) about two years after the mainshock. Spectral ratios are calculated between all combinations of events that both occurred close to one another and had similar mechanisms. We calculated seismic energies of P and S waves for each event by fitting omega-square spectral models to the spectral ratios. Analysis of both the high and lower sampling rate data results in statistically significant size dependence of E_s/M_o; however, none of these trends can explain overall scaling when all events, including the mainshock, are considered. Artificial size dependence due to band limitation and omega-square assumption may be responsible for the apparent trends.

Key words: Seismic energy, spectral ratio, high-sampling data, Hi-net.

1. Introduction

Seismic energy E_s, energy radiated from seismic sources and carried by seismic waves, is a fundamental quantity that characterizes dynamic processes of earthquake rupture. Unlike static parameters like seismic moment M_o, it is not possible to estimate E_s for a single station over a narrow range of frequency. Since both the spatial distribution of stations and frequency bands are limited for most earthquakes, estimation of E_s is typically subject to large errors. Nevertheless, many studies have determined E_s and discussed the implications of the observed scaling of the ratio E_s/M_o or apparent stress: E_s/M_o multiplied by the rigidity (e.g., Kanamori *et al*., 1993; McGarr, 1999). As discussed by Ide and Beroza (2001) and Ide *et al*. (2003), there are several factors that affect the estimation of seismic energy, especially for small events. These are insufficient frequency bandwidth, event selection bias, and improper modeling of crustal attenuation structure. In most cases, these factors can have the effect of introducing artificial trends in which small earthquakes tend to have low seismic energy. Thus, the possible size dependence of E_s/M_o remains a research issue.

Because they provide records of earthquake ground motion before it propagates through the heterogeneous and highly attenuating near surface, high-sample rate records from deep boreholes provide some of the most valuable data for the study of small earthquakes as shown in: Cajon Pass (Abercrombie, 1995), Long Valley, California (Prejean and Ellsworth, 2001) and Ohtaki, Japan (Matsuzawa *et al*., 2004). Such deep boreholes are quite rare, however, and are only available in a few select locations. There are, however, many more recordings of earthquakes from somewhat shallower boreholes. Data from shallow boreholes have many of the same advantages that records from deep boreholes have for estimating energy. There are about 700 shallow borehole seismic stations in Hi-net (Obara, 2002), Japanese national seismometer network maintained by National Research Institute for Earth Science and Disaster Prevention (NIED). In addition to regular 100 sample per second (sps) records of Hi-net that are distributed via the Internet, there are also high-sample rate records available that record at 1000 (1k) sps. We first analyze these data for the study of seismic energy.

Although there are many studies of seismic energy, the difference in techniques, differences in tectonic environments, and the large uncertainties in its measurement make direct comparisons between studies difficult. Therefore, it is desirable to compile events of wide size range within a small area of uniform tectonic conditions and to analyze them as uniformly as possible. An earthquake of M_w 6.6 occurred on October 6, 2000 in the western part of Tottori Prefecture, Japan (Fig. 1) providing a good data set for this purpose. The mainshock and aftershocks are recorded by Hi-net and KiK-net, a strong-motion seismometer network that uses the same boreholes as the Hi-net. In this study we focus on aftershocks within a small area that had large slip during the mainshock.

Izutani and Kanamori (2001) estimated E_s for the mainshock and an M_w 3.9 aftershock using strong-motion data and spectral ratio analysis. Combining with the results for three other earthquakes, they conclude that small earthquakes have small E_s/M_o ratio. One objective of the present

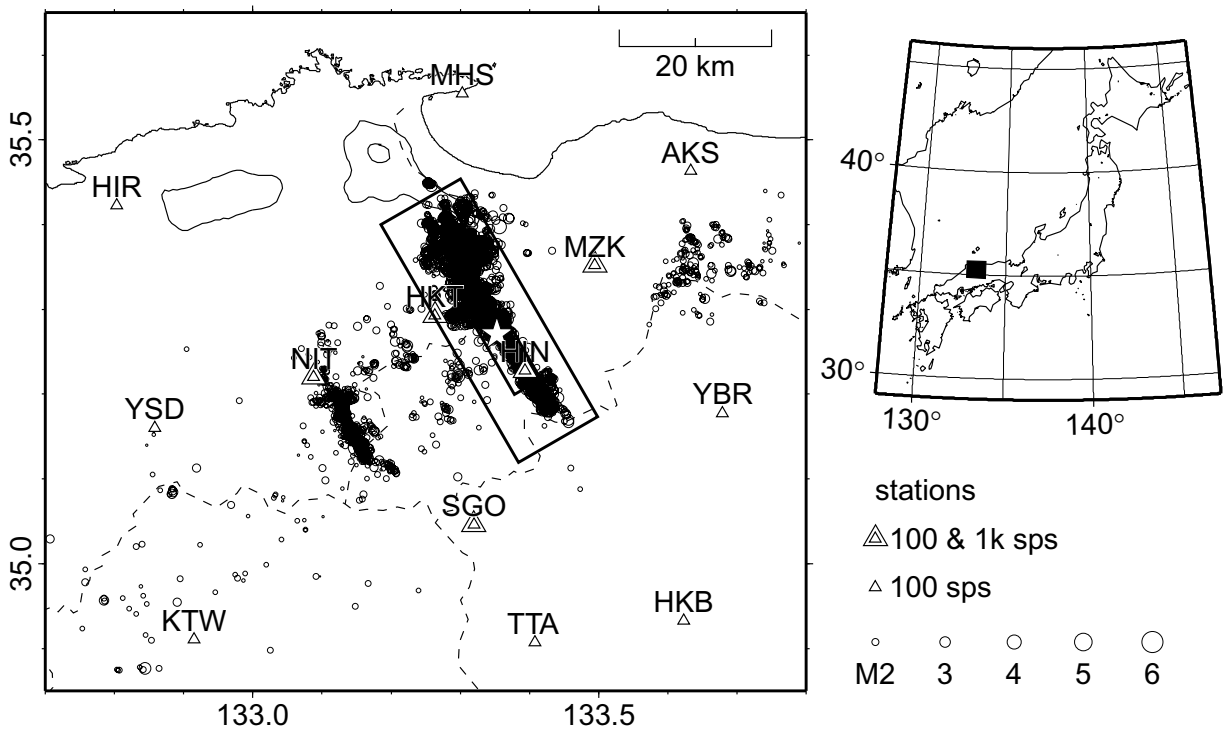

Fig. 1. Location of study area and station distribution. Hypocenters determined by JMA in October 2000 are shown by circles. Triangles are stations and double symbols indicate stations where 1k sps data are available. Rectangular area is magnified in Fig. 2.

Table 1. Stations used.

Data	Code	Well depth (m)	Vp (m/s)	Vs (m/s)
100 & 1k	HKT	104	5300	2800
	HIN	103	2600	790
	MZK	203	4600	2000
	SGO	103	4600	2100
	NIT	104	3800	1200
100 only	MHS	203	3840	1570
	YBR	103	4400	2400
	AKS	210	2550	1350
	YSD	103	4570	2050
	TTA	103	4200	1800
	HKB	103	4650	2250
	KTW	103	3600	1650
	HIR	203	3550	1740

study is to see whether or not this trend continues down to the smallest observable events. Exploitation of high-sample rate data allows us to analyze small events down to about M 0.5. In this paper, we estimate the seismic energy of the aftershocks using Hi-net records and a spectral ratio analysis method with the assumption of an omega-square model. Comparing for a wide range of event size, we can discuss the E_s/M_o scaling with more confidence. In the following, at first, we analyze each data set in a relatively narrow range of event size and reach a tentative conclusion that there is some size dependence of E_s/M_o. However, what is surprising and important in studies of earthquake scaling is that none of this trend is consistent with the overall E_s/M_o distribution.

2. The Data Set of the 2000 Western Tottori Earthquake

Figure 1 shows the locations of the mainshock and the aftershocks of the Western Tottori earthquake together with the station distribution of Hi-net used in this study (Table 1). Each station has a three component high-sensitivity seismometer in a borehole at depths ranging from 100 m to 200 m. Paleocene granites dominate most of the area in Fig. 1 and all stations are located within hard rock with high seismic wave velocity at the seismometer depth as shown in Table 1. Each seismometer has a pendulum frequency of about 1 Hz and its damping constant is tailored to be 0.7.

Regular Hi-net data, as continuous or triggered records, are available via the Internet. The sampling rate of these

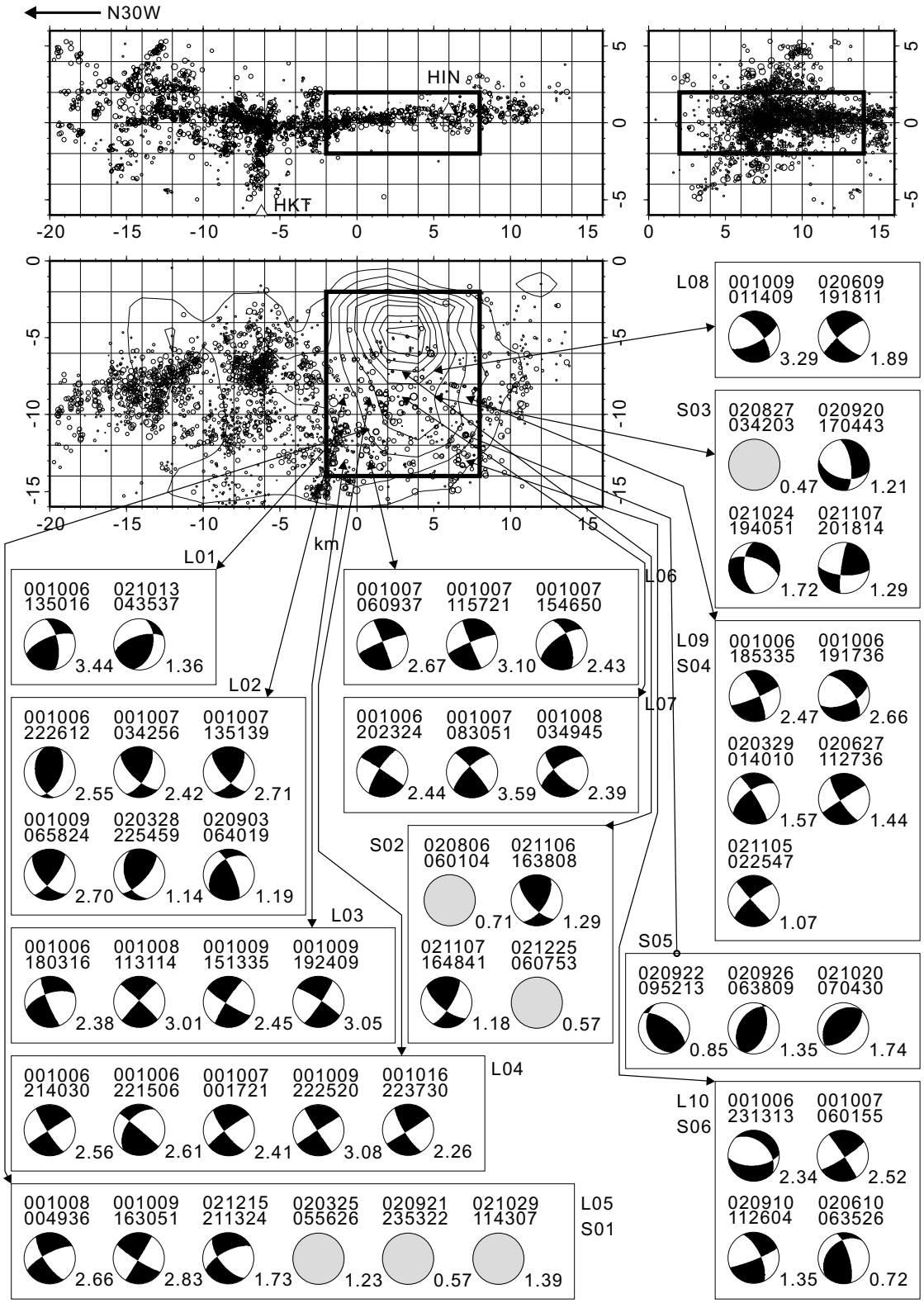

Fig. 2. Hypocenter distribution. Map view (top left) and two cross sections (top right and middle left). Contours are slip distribution determined by Wu (2004). Contour interval is 0.5 m. Bold rectangles show studied space in which event pairs are compiled for each $2 \times 2 \times 2$ km^3 cell. Beach balls grouped for each cell (bottom) show the mechanism of all analyzed events. S01–S06 and L01–L10 are the group IDs and each ID corresponds to one cell. Each event is identified by date and time shown at the top of the beach ball and its moment magnitude is shown at right bottom corner. The mechanisms of some small events are unknown and gray circles are located instead of beach balls.

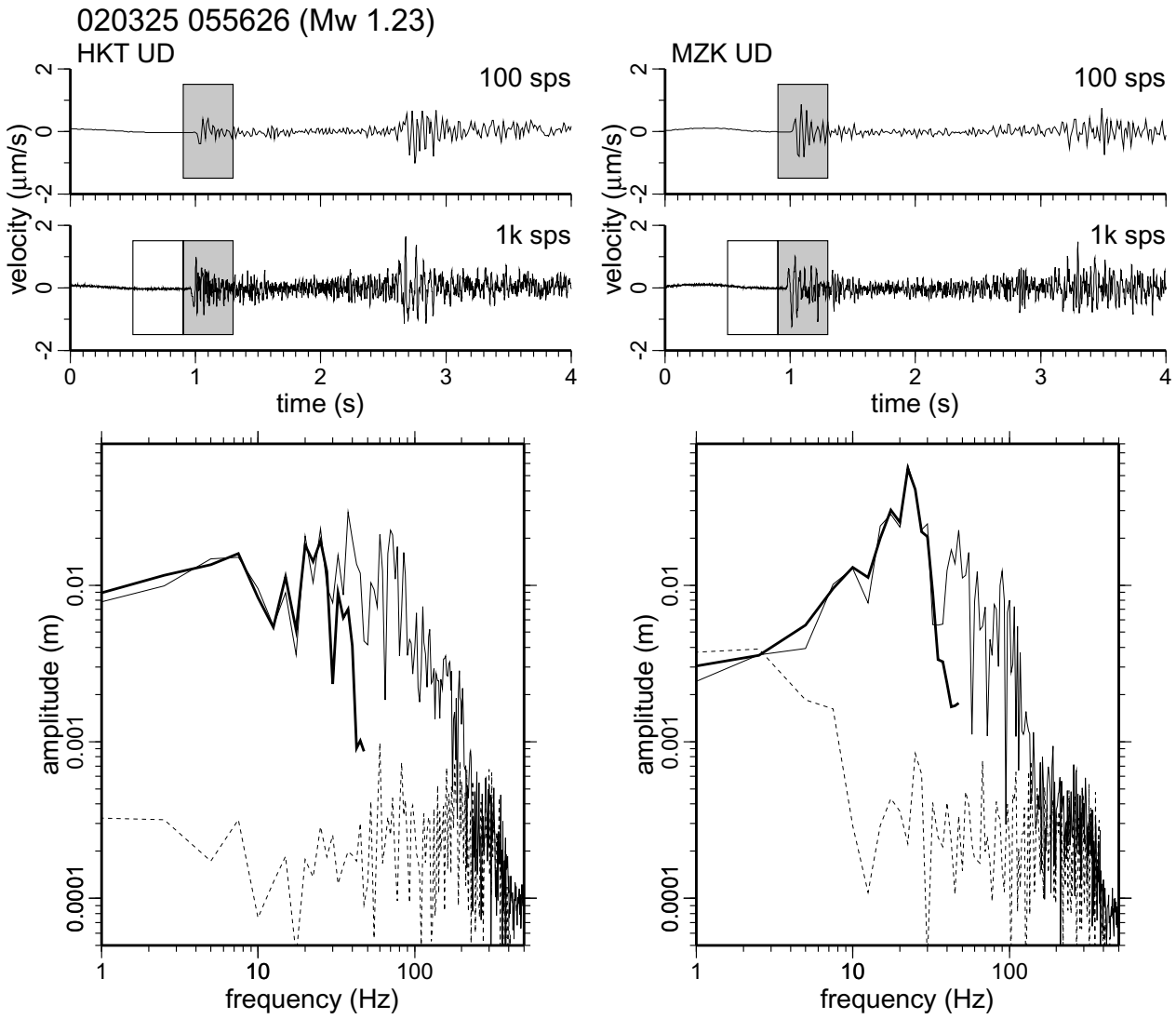

Fig. 3. Examples of observed data. 100 sps and 1k sps data at station HKT and MZK for one M_w 1.23 event. Top figures compare two data in time domain and bottom figures show amplitude of their velocity spectra. Bold, thin, and dotted lines represent 100 sps signal, 1k sps signal, and 1k sps noise, respectively, which are calculated in the time window shown above. Gray rectangles are signal windows and an open rectangle is noise window.

regular data is 100 sps. In addition to these data, each Hi-net station can keep records at higher frequency of 1k sps, as produced by a decimation process from the original sampling rate of 2k sps. The dynamic range of the 1k sps record is 24 bits. The 1k sps record are decimated to 100 sps data with 27-bit precision and sent to the data centers for distribution. The 1k sps data are routinely discarded after decimation. Because these data are not routinely archived, there are no high-sample rate recordings of aftershocks immediately after the mainshock. The recording of 1k sps data started at the five stations listed in Table 1 from March 2002, one and a half years after the mainshock. Two of the five stations, HKT and HIN, are located within the aftershock epicentral area. Although there are data at NIT, they are not used for spectral ratio analyses because of their poor quality. Also, because of technical problems of data transfer, data for many events are less complete than the regular data set.

In this study, we use both 100 sps data and 1k sps data for two periods: 1) two weeks from the mainshock, from October 6, 2000 to October 18, 2000 and 2) two years later, from March 20, 2002 to December 31, 2002. 100 sps data are available in both periods and 1k sps data are available only in the latter. The distributions of event sizes are also different during these two periods. The maximum events analyzed in the first and second periods are M_w 3.6 and 1.9, respectively.

To obtain better relative locations, we relocated the hypocenters using the catalog arrival times determined by Japan Meteorological Agency (JMA) and the double-difference method of Waldhauser and Ellsworth (2000). Although there is a systematic difference of up to 2 km between hypocenters of two periods due to the different station distribution in the original JMA catalog, this procedure reduced the difference and the two distributions are qualitatively similar. Figure 2 shows the relocated hypocenters.

The aftershock area of the western Tottori earthquake extends about 30 km in a NNW-SSE direction. The area of large mainshock slip is restricted to a small part of the total aftershock area. Contours in Fig. 2 show the final slip distribution of the mainshock determined using strong motion records by Wu (2004). The area of large slip is located in the

southeast and shallow part of the aftershock distribution. To minimize any possible differences in our measurements or in earthquake behavior due to differences in location, we focus our attention on this area of large slip as shown by bold lines in Fig. 2. Aftershocks in this area form a single plane, which is not true for many of the widely distributed hypocenters outside of this area.

We divided this volume into small cubic cells of $2 \times 2 \times 2$ km^3 and made event groups for each cell. This grouping was based on the focal mechanisms, which were determined using polarities and amplitudes of P and SH waves of the 100 sps data as shown in Fig. 2. Together with the mechanism, scalar seismic moment was estimated for each event using the lower frequency limit of displacement spectrum. There are large uncertainties in the mechanism of the smaller events. In cases where the mechanism is not well determined, we just compare waveforms of all available components directly. Since spectral ratio analysis requires some separation of seismic moments and corner frequencies, we adopted only groups in which the maximum moment difference between events is larger than an order of magnitude. This criterion is too strict for 1k sps data and we loosen it to a factor 5 for the smaller event groups. Nevertheless, there are only six groups that satisfy the above criteria for 1k sps data.

Figure 3 shows examples of the 1k sps data compared to the regular 100 sps data for the vertical component of velocity from a M 1.2 event at a typical distance from stations HKT and MZK. The apparent difference of P arrival time is an artifact due to digital filtering. Fourier spectral amplitudes of the signal and pre-event noise windows for these records show that the available bandwidth is generally up to 200 Hz for both stations HKT and HIN. For more distant stations, MZK, and SGO, the highest available frequency is somewhat lower at about 100–150 Hz. In the horizontal records, there are occasionally strange oscillating signals, which may arise from the coupling between the seismometer and borehole wall. Since the actual source of this signal is not clear, and it is improper to use these records without care, we carried out analysis of 1k sps data mainly based on P-wave part in vertical component and use SH-wave part in horizontal component for comparison. In the analysis of 100 sps data, both the P-wave part in the vertical component and SH-wave part in horizontal components are used.

3. Spectral Ratio Analysis Method

We used the spectral analysis method which is basically the same as that used in the study of small earthquakes in Long Valley, California by Ide *et al.* (2003). This method is an extension of the multiple empirical Green's function method proposed by Hough (1997). First we review this analysis method.

The main assumption of this method is that a source spectrum is approximated by an omega-square model. The displacement spectrum $u(f)$, following Boatwright (1978), is proportional to

$$\frac{M_o}{\sqrt{1+(f/f_c)^4}}, \tag{1}$$

where f_c is the corner frequency. As discussed by Ide *et al.* (2003), the assumption of an alternative omega-square model of Brune (1970) yields similar results; however, Eq. (1) better simulates the sharp corners in our observed spectra. The logarithm of the ratio between two displacement spectra $u^1(f)$ and $u^2(f)$;

$$\log u^1(f) - \log u^2(f) = \log M_o^1 - \log M_o^2 + \frac{1}{2}\log\frac{1+\left(f/f_c^2\right)^4}{1+\left(f/f_c^1\right)^4} \tag{2}$$

are the data that were used to estimate the corner frequency and log seismic moment of each event.

Figure 4 shows an example of the spectral analysis. For each original velocity record (Fig. 4(a)), we first calculate Fourier spectral amplitudes using time windows, which are 0.4 s for 1k sps data and 4.0 s for 100 sps data, respectively. In the case that S waves are included in P wave window, we shorten it not to include S waves. The spectrum is resampled at equal intervals in frequency, $\log f = 0.05$, 20 points over one decade of frequency (Fig. 4(b)). Then we take the spectral ratio for all combinations of events in the group (Fig. 4(c)). The change of the time window makes slightly different spectra, but has little effect on the spectral ratio. As long as the same time windows are used for two events of similar mechanisms and locations, the waves included in the window, a direct wave as well as reflected, refracted and coda waves, should be almost identical and the ratio between them is basically the source spectral ratio that we are interested in, which is common for all waves.

The calculated spectral ratio is then inverted for log seismic moments and corner frequencies using Eq. (2) (Fig. 4(c)). Each data sample is differently weighted according to signal to noise ratio. When there are N events available, there are $2N$ unknown parameters: N seismic moments and N corner frequencies. These are determined using $N(N-1)/2$ spectral ratio measurements. The frequency bandwidth actually available is less than 200 Hz as noted in the previous section. Therefore we limited the frequency range from 2.5 to 200 Hz and 0.25 to 30 Hz for 1k sps and 100 sps data, respectively. There are approximately 40 data points in each spectral ratio. Although the number of the data is larger than that of parameters, the problem is underdetermined and we need another constraint to determine all parameters. We applied a constraint to fix the average of all log seismic moment to be the same as that obtained by the mechanism analysis in the previous section $M^i_{o\_\mathrm{mech}}$,

$$\sum_{i=1}^{N}\log M_o^i = \sum_{i=1}^{N}\log M^i_{o\_\mathrm{mech}}. \tag{3}$$

These equations are solved as a linearized nonlinear least square problem using the Levenberg-Marquart method. To minimize possible dependence on initial values, we use at least 20 randomly generated initial values for each inversion.

Once the parameters are determined, the difference between the observed spectrum and calculated omega-square model is assumed to represent the effects, such as attenuation, elastic propagation, site amplification and instrumental response, which are canceled by taking the spectral ratio. We refer to the collective effects of these as the average attenua-

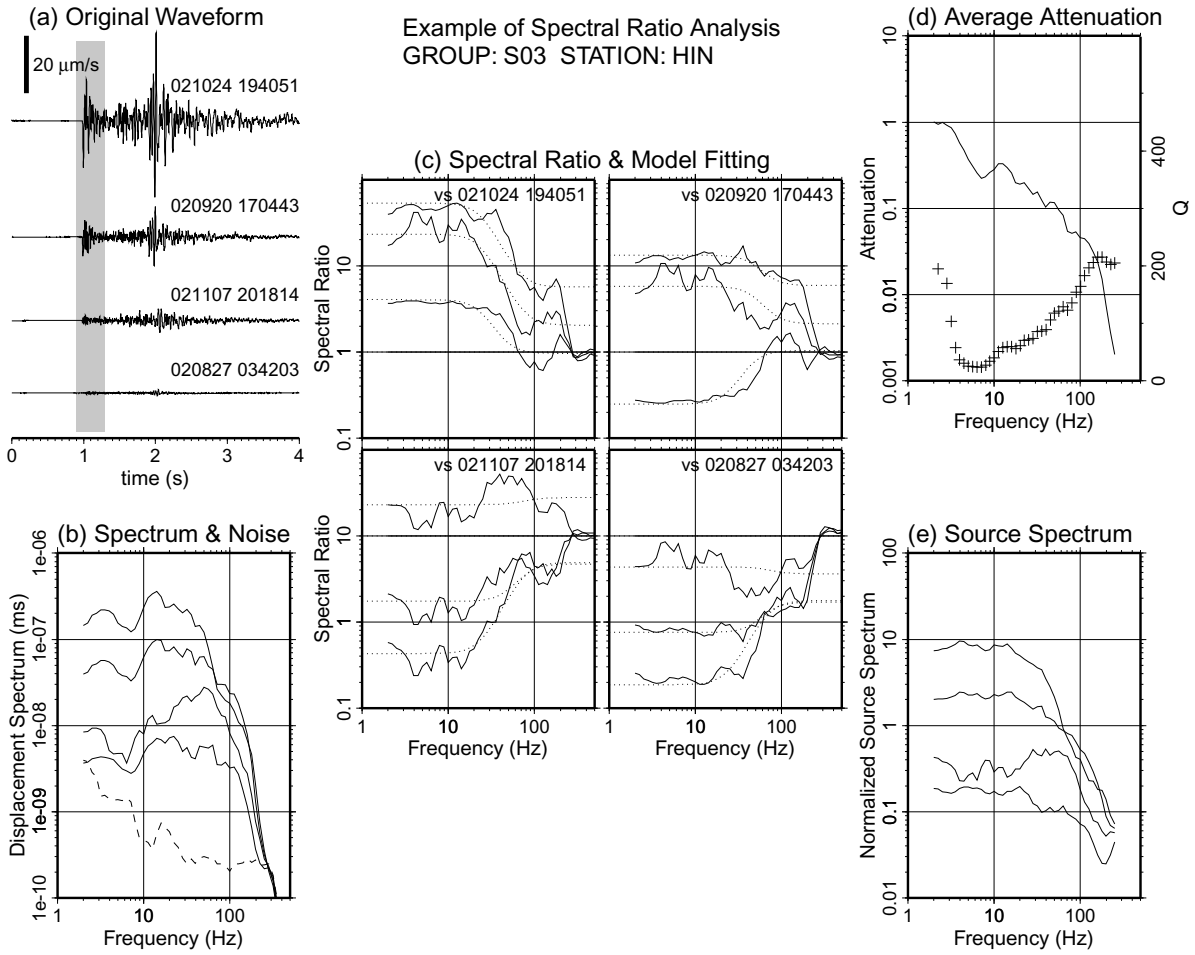

Fig. 4. Example of an analysis sequence. A group of four events is analyzed using P waves of 1k sps data at station HIN. (a) Waveforms with 0.4 s time window for P-wave signals. (b) Resampled spectral amplitude. Solid lines are data and a dashed line shows the noise level of the minimum event. (c) Fitting of spectral ratio by omega-square curves. Each figure shows ratio to one event. Dotted lines are ratios calculated using the fitted models. (d) Average attenuation (solid line, left axis). Each cross represents Q value at each frequency (right axis). (e) Source spectra (normalized moment rate spectra) of four events.

tion function, which is defined by,

$$\frac{1}{N}\sum_{i=1}^{N}\left[\log u^i(f) - \log M_o^i + \frac{1}{2}\log\left(1+\left(f/f_c^i\right)^4\right)\right]. \quad (4)$$

Figure 4(d) shows the example of this function normalized at the lowest frequency. The source spectrum (Moment rate spectrum), $|\dot{M}_o(f)|$, is the difference between this average attenuation and data spectrum and close to the assumed omega-square model (Fig. 4(e)). Seismic energy of P and S waves are then calculated using this spectrum as

$$E_s^c = \frac{1}{A_c \pi \rho V_c^5}\int \left|\ddot{M}_o(f)\right|^2 df, \quad (5)$$

where c is P or S. $A_P = 15$ and $A_S = 10$. In this calculation we assumed that $V_P = 6000$ m/s, $V_S = 3464$ m/s, and $\rho = 2500$ kg/m^3. The missing part of the energy is added based on the assumption of omega-square model, as described in Ide and Beroza (2001). The above procedure gives energy values for all events in one event group, based on a single station and either P or S waves. In this calculation it is assumed that each source is a point source and the moment rate function has no directivity. Of course this assumption is not adequate and the estimated energy at each station will be affected by any directivity effect that is present in the data. Directivity represents an unmodeled source of error that we try to minimize by estimating the seismic energy as a linear average of the individual estimates at each station.

4. Result of Seismic Energy Estimation

4.1 100 sps data

First let us look at the events in the first interval, about two weeks after the mainshock, analyzed using 100 sps data set. There are 10 cells that contain events with enough magnitude difference, similar mechanisms and locations. Figure 5 shows examples of spectral fits. For some small events, the estimated corner frequency is merely the lower limit and the real one is probably higher than it. However, for events larger than M_w 2, the fitting seems to be quite good. Because not resolving the corner frequency of the smaller events affects the estimation of seismic energies, we did not calculate energy for events smaller than M_w 2 using 100 sps data.

Table 2 summarizes the estimated values of E_s by its average and standard deviation in a logarithmic scale. Figure 6 shows the values of E_s/M_o ratios and the corner frequencies compared to seismic moments. The seismic moment is deter-

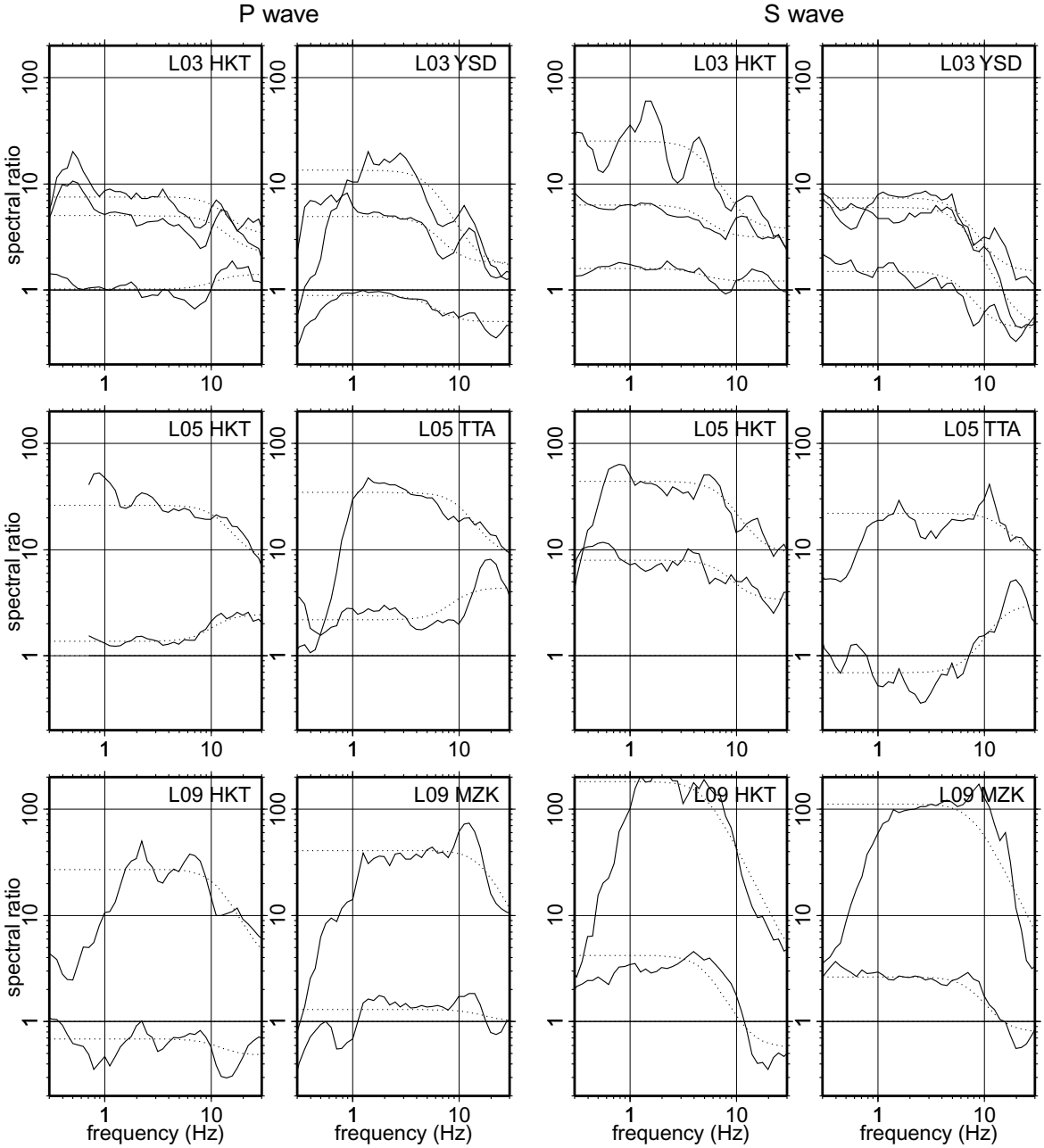

Fig. 5. Example of spectral fitting (100 sps) for P-waves (left figures) and S-waves (right). Each figure shows ratios of the largest event to others in each group. Solid lines are data and dotted lines are model predictions. Group ID and station name are shown in the upper left corner.

mined by the lowest frequency level of displacement spectra. In the E_s/M_o plot, a straight line shows the maximum and the minimum estimate of seismic energy for each event and a circle represents their arithmetic mean. The value at the closest station HKT is shown by triangle for comparison with the 1k sps results. It is unfortunate that the data of another closest station, HIN, is not available in this period because of trouble with the electronics.

The energies of P waves are smaller by about one order of magnitude than the energies of the S waves. According to Boatwright and Choy (1986) the ratio of E_s^S/E_s^P is typically 15.6. If this ratio is quite large or small for an event, it is likely that the estimate of either E_s^P or E_s^S is erroneous. Therefore if E_s^S/E_s^P is larger than 100 or smaller than 3, we did not use the event in the following discussion. Since the upper limit of the analysis is 30 Hz and the estimates of corner frequency are close to this frequency, artificial upper limits of E_s/M_o that scale with seismic moment below M_w 2.5 are evident in both graphs, despite the fact that the corner frequencies seems to be resolved well in Fig. 5. Even if some events are missing in this region, the major trend seems to be unchanged. The least squares fittings of a line for the relation between $\log E_s/M_o$ and $\log M_o$ yields trends of 0.56 both for P and S waves. The standard deviation is 0.10 and 0.18 for P and S waves, respectively. Therefore, the trend is statistically significant and the hypothesis of constant E_s/M_o can be rejected from these observations. This trend is, however, not consistent with overall trend which will be apparent in the rest of this section.

Table 2. Earthquakes anlyzed (low frequency).

ID	date (JST)	time (JST)	Lat. (°N)	Lon. (°E)	Dep. (km)	M_w	E_s^P (J)	NP†	E_s^S (J)	NS‡	E_s^S/E_s^P
L01	001006	135016	35.2845	133.3491	13.1	3.44	4.06e + 09	7	6.28e + 10	9	15.5
L01	021013	043537	35.2768	133.3519	12.3	1.36	—	—	—	—	—
L02	001006	222612	35.2821	133.3435	10.3	2.55	1.65e + 06	4	2.39e + 08	6	145
L02	001007	034256	35.2803	133.3435	11.5	2.42	3.00e + 06	4	1.27e + 08	6	42.3
L02	001007	135139	35.2755	133.3466	10.7	2.71	1.48e + 06	4	1.60e + 08	6	108
L02	001009	065824	35.2818	133.3436	11.1	2.70	1.58e + 07	4	5.79e + 08	6	36.6
L02	020328	225459	35.2777	133.3367	11.8	1.14	—	—	—	—	—
L02	020903	064019	35.2840	133.3419	11.6	1.19	—	—	—	—	—
L03	001006	180316	35.2839	133.3370	13.8	2.38	8.02e + 06	6	7.46e + 07	6	9.30
L03	001008	113114	35.2813	133.3406	12.9	3.01	2.55e + 08	6	5.40e + 08	6	2.12
L03	001009	151335	35.2837	133.3379	12.4	2.47	2.43e + 07	6	5.95e + 07	6	2.45
L03	001009	192409	35.2816	133.3402	13.1	3.02	3.56e + 08	6	2.73e + 09	6	7.67
L04	001006	214030	35.2592	133.3629	9.4	2.56	1.17e + 07	6	1.11e + 08	8	9.49
L04	001006	221506	35.2651	133.3617	8.3	2.61	2.46e + 06	6	5.84e + 07	8	23.7
L04	001007	001721	35.2586	133.3681	8.7	2.41	2.02e + 06	7	1.86e + 07	8	9.21
L04	001009	222520	35.2599	133.3612	8.6	3.08	3.54e + 07	7	5.55e + 08	8	15.7
L04	001016	223730	35.2572	133.3643	9.9	2.26	1.03e + 06	6	1.29e + 07	7	12.5
L05	001008	004936	35.2650	133.3616	11.6	2.66	1.82e + 07	8	1.96e + 08	6	10.8
L05	001009	163051	35.2618	133.3612	11.1	2.83	6.67e + 07	8	1.40e + 09	6	21.0
L05	021215	211324	35.2707	133.3545	11.4	1.73	—	—	—	—	—
L06	001007	060937	35.2592	133.3674	12.5	2.67	1.41e + 07	6	8.53e + 07	6	6.05
L06	001007	115721	35.2671	133.3586	12.3	3.10	3.09e + 08	6	1.22e + 09	6	3.95
L06	001007	154650	35.2694	133.3558	12.7	2.43	1.19e + 07	6	9.73e + 07	6	8.18
L07	001006	202324	35.2441	133.3795	9.5	2.44	8.89e + 06	10	1.61e + 08	9	18.1
L07	001007	083051	35.2442	133.3778	8.8	3.59	1.89e + 09	10	2.17e + 10	10	11.5
L07	001008	034945	35.2519	133.3766	9.3	2.39	7.84e + 06	10	8.29e + 07	10	10.6
L08	001009	011409	35.2354	133.3837	6.0	3.29	9.61e + 08	9	1.20e + 10	7	12.5
L08	020609	191811	35.2420	133.3852	7.6	1.89	—	—	—	—	—
L09	001006	185335	35.2265	133.3962	9.8	2.47	1.30e + 07	7	3.28e + 08	5	25.2
L09	001006	191736	35.2256	133.3960	8.1	2.66	6.05e + 06	7	9.28e + 07	5	15.3
L09	020627	112736	35.2219	133.4033	8.2	1.44	—	—	—	—	—
L10	001006	231313	35.2196	133.3955	13.3	2.34	1.73e + 07	7	7.26e + 07	6	4.20
L10	001007	060155	35.2218	133.3946	12.9	2.52	3.35e + 07	7	1.00e + 08	7	2.99
L10	020910	112604	35.2138	133.4027	12.1	1.35	—	—	—	—	—

†Number of stations used for E_s^P estimation. ‡Number of stations used for E_s^S estimation.

4.2 1k sps data

There are just six groups of events for 1k sps data. Although data are available for five stations, for many small events, only one station, HKT or HIN, is available and we cannot take averages among multiple estimates. Figure 7 shows almost all cases of the spectral fitting procedure for P waves. Fitting is successful in most cases. Here again, although the corner frequencies of small events are within the analysis frequency range, it is uncertain whether these values are well resolved.

Table 3 summarizes the result of the analysis of 1k sps data and Fig. 8 compares the E_s/M_o ratio and corner frequencies with the seismic moments. In this case, we do not refer E_s^S/E_s^P because E_s^P is more reliable than E_s^S. The symbols are the same as Fig. 6. Again, there is an artificial upper limit at 200 Hz. Because of the small number of stations, the difference between the maximum and the minimum of E_s/M_o seems to be small. This just reflects the lack of the data rather than small variance. To make a fair comparison between Figs. 6 and 8, we should look at triangle symbols, which are the estimate based on only the station HKT, in both figure. A comparison reveals that the distributions are at least qualitatively similar.

Statistically, the slope of the least squares fittings is $0.26\pm$

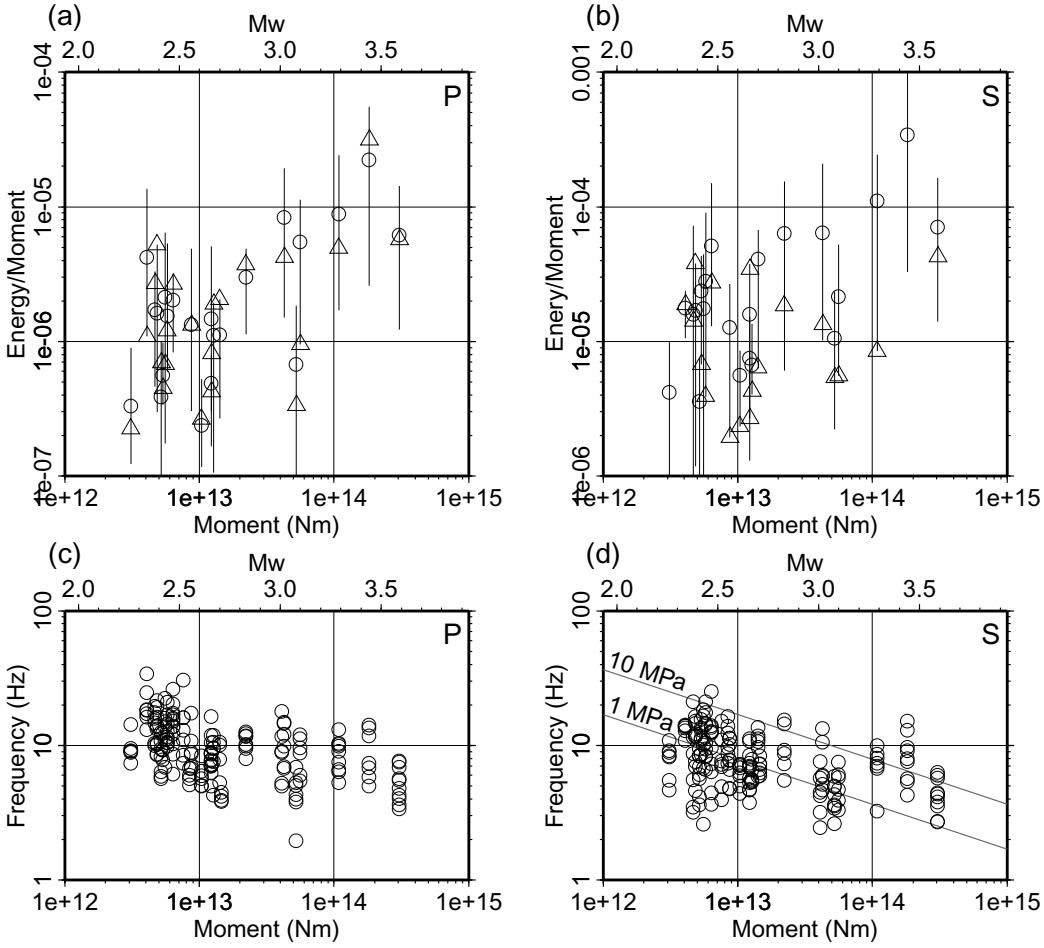

Fig. 6. The scaling relations determined from 100 sps data. (a) Comparison between E_s/M_o and seismic moment for P wave. Circles are average estimates and triangles are estimates at station HKT. Bar extends from the maximum to the minimum values for each event. (b) Same for S-wave. (c) Comparison between corner frequency f_c and seismic moment. (d) Same for S-wave. Gray lines show constant Brune stress drop (Brune, 1970) condition.

0.23 and 0.46 ± 0.11 for P and S waves, respectively. As noted previously, the spectra of S-waves from the horizontal components are less reliable for these frequencies. The artificial upper limit of 200 Hz affects more than the 100 sps result. Therefore, although there is a similar trend of increasing E_s/M_o with increasing M_o, it is less significant than the result for 100 sps data.

4.3 E_S/M_O ratio in wide range

Izutani and Kanamori (2001) estimated E_s of the mainshock and an aftershock of M_w 3.9 using the strong motion records of K-net and KiK-net. They also used spectral ratio of S-waves between these two events. Their method differs from our method in that they assumed a more general type of spectral model, fixed the difference of seismic moments, and estimated the energy as an average of spectrum of all stations. Although the assumed spectral model is different, the result of their analysis indicates that the spectral slope at higher frequencies is -1.9, close to omega-square model we assume. Most slip of the mainshock occurred in our study area. The M_w 3.9 aftershock occurred slightly outside of our study area. Therefore, the difference of study condition between two studies is not significant and it should be useful to compare their result with ours.

To ensure that this comparison is meaningful, we estimated the seismic moment and the seismic energy for this aftershock using the method of this study. The seismic moment is 4.9×10^{14} Nm, which is smaller than the estimates of Izutani and Kanamori (2001), 7.6×10^{14} Nm, by a factor of 1.5. The estimated E_s/M_o varies from 10^{-6} to 10^{-4} for each station and the average is 1.8×10^{-5}, which is comparable with 0.54×10^{-5} of Izutani and Kanamori (2001). Although the error is large, estimates of two studies are at least in the same order.

Figure 9 compares their results with all the results in this study. To correct for the unmodeled S-wave energy for the events in this study, seismic energies of P-waves are plotted after being multiplied by a factor of 10, since they are more reliable in the 1k sps analysis. Comparison over this wide range reveals a size dependence in E_s/M_o in each frequency range, which seems to be significant at least for 100 sps data, but forms an echelon-like structure with an inconsistent moment dependence overall. An alternative interpretation is that E_s/M_o is constant for these data at a value of $\approx 3 \times 10^{-5}$ with about one order variation for individual estimates. The least-square trend for these data is -0.019 ± 0.057. Therefore, the hypothesis that E_s/M_o is constant cannot be rejected from these observations.

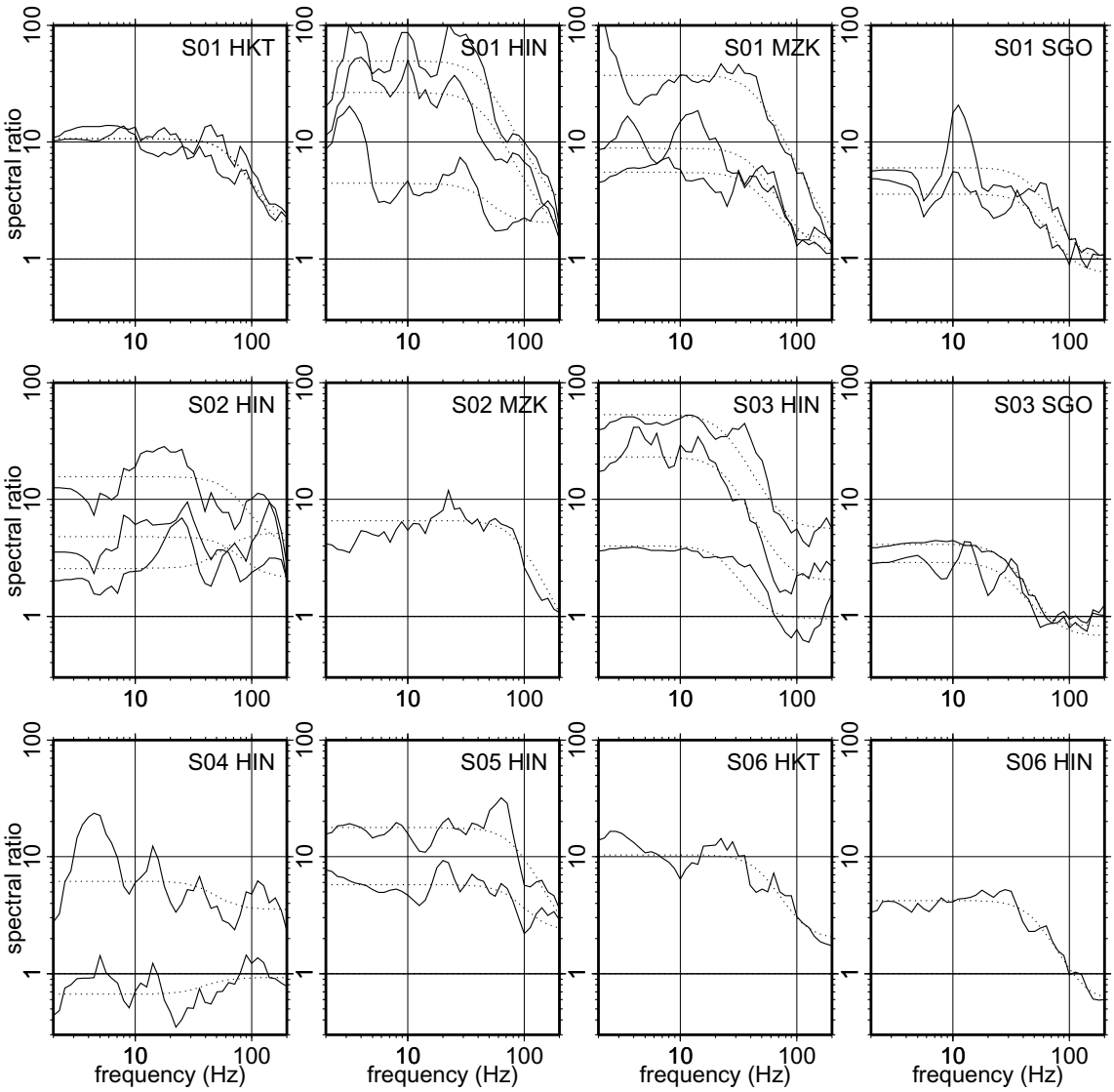

Fig. 7. Example of spectral fitting (1k sps). All ratios are for P-waves. Each figure shows the ratios to the largest event in each group. Solid lines are data and dotted lines are model predictions. Group ID and station name are shown in the upper right corner.

5. Discussion

The echelon-like structure of the observations from the two data sets needs some explanation. One possibility is that it is just an artifact due to either a limitation of the data or inappropriate model assumptions. Another is that this represents some real phenomena. We now consider both possibilities.

As described by Ide and Beroza (2001), the limited bandwidth can lead to an artificial trend. Spectral fitting at frequencies close to the higher frequency limit, 30 Hz for 100 sps and 200 Hz for 1k sps, may not be very reliable. However, for 100 sps data, we have some events with corner frequencies that are almost in the middle of the analysis range and show small E_s/M_o ratios. Although we may exclude some small events of small E_s/M_o because of poor resolution at high frequencies, others remain and cannot be explained as artifacts due to limited bandwidth. For 1k sps data the trend is not significant and the corner frequencies of most events having small E_s/M_o are located near the upper limit of analysis range. Therefore the trend in these data could be attributed to an artifact of limited bandwidth.

In this study, we used a simple assumption of an omega-square model. This assumption is frequently used but may not hold, especially for small events. This assumption could lead to artificial size dependence that is just visible in each narrow frequency range. When the actual slope is smaller than two, the assumption of an omega-square spectrum leads to a high estimated corner frequency for the smaller events and has just the opposite effect for the larger events. The net result would be an artificial increase of E_s/M_o with increasing moment. There are some events with slopes that seem to be less than two, but it is not easy to confirm that slope is generally less than 2 for these events because the bandwidths of both 100 sps and 1k sps data are not sufficient. If there were events of M 3–4 recorded at 1k sps, a direct assessment of high-frequency slope would be feasible.

We also cannot exclude the possibility that this echelon structure reflects real phenomena. The two data sets are obtained in different periods and average E_s/M_o ratio in the first period is smaller than that of the second period. It is re-

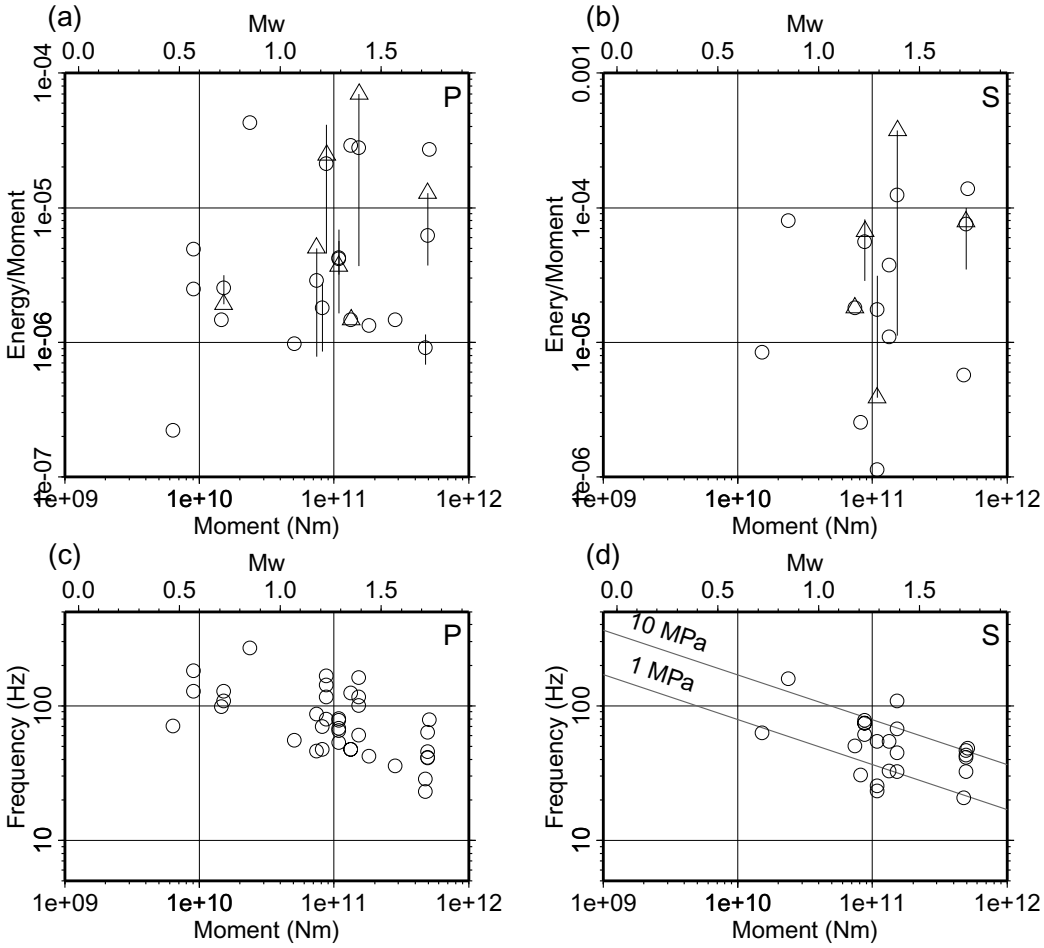

Fig. 8. The scaling relations determined from 1k sps data. (a) Comparison between E_s/M_o and seismic moment for P wave. Circles are average estimates and triangles are estimates at station HKT. Bar extends from the maximum to the minimum values for each event. (b) Same for S-wave. (c) Comparison between corner frequency f_c and seismic moment. (d) Same for S-wave. Gray lines show constant Brune stress drop (Brune, 1970) condition.

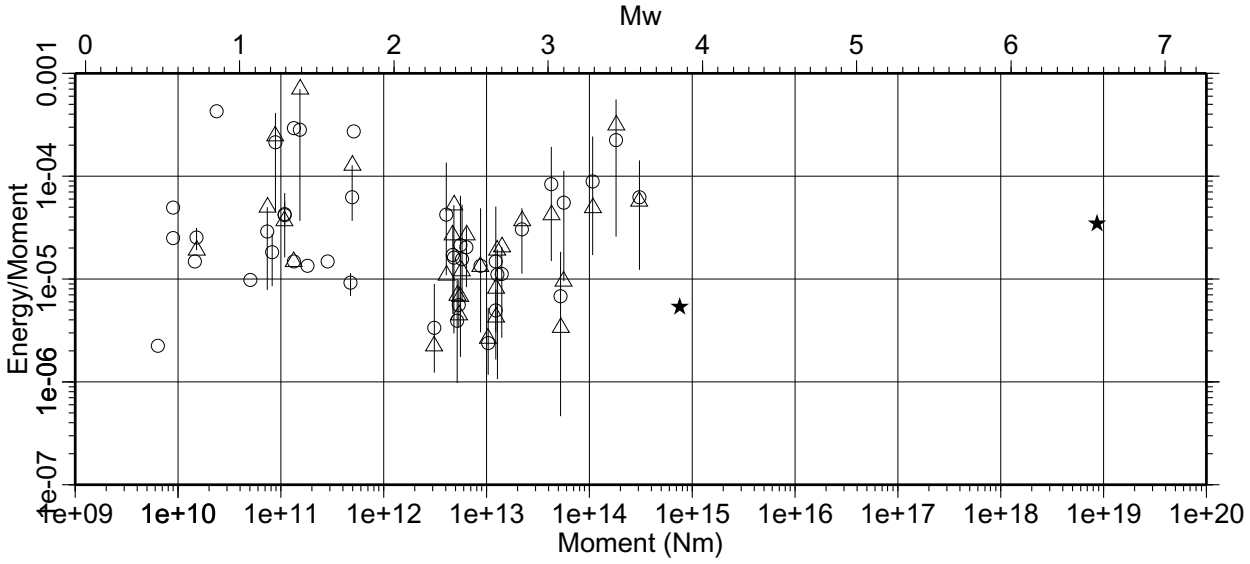

Fig. 9. Comparison between the ratio E_s/M_o and seismic moment M_o. Circles are energy estimates using P-waves multiplied by 10. Circles are average estimates and triangles are estimates at station HKT. Bar extends from the maximum to minimum values for each event. Two stars indicate the E_s/M_o values of the mainshock and one aftershock estimated by Izutani and Kanamori (2001).

Table 3. Earthquakes anlyzed (high frequency).

ID	date (JST)	time (JST)	Lat. (°N)	Lon. (°E)	Dep. (km)	M_w	E_s^P (J)	NP†	E_s^S (J)	NS‡
S01	020325	055626	35.2590	133.3656	11.7	1.23	1.88e + 06	4	4.95e + 06	4
S01	020325	055626	35.2590	133.3656	11.7	1.23	1.88e + 06	4	4.95e + 06	4
S01	020921	235322	35.2726	133.3570	11.3	0.57	4.44e + 04	1	—	—
S01	020921	235322	35.2726	133.3570	11.3	0.57	4.44e + 04	1	—	—
S01	021029	114307	35.2702	133.3558	11.1	1.39	4.30e + 06	4	1.90e + 07	4
S01	021029	114307	35.2702	133.3558	11.1	1.39	4.30e + 06	4	1.90e + 07	4
S01	021215	211324	35.2707	133.3545	11.4	1.73	3.10e + 06	4	3.74e + 07	4
S01	021215	211324	35.2707	133.3545	11.4	1.73	3.10e + 06	4	3.74e + 07	4
S02	020806	060104	35.2554	133.3734	6.4	0.71	2.16e + 04	1	—	—
S02	020806	060104	35.2554	133.3734	6.4	0.71	2.16e + 04	1	—	—
S02	021106	163808	35.2503	133.3815	7.4	1.29	4.52e + 05	3	1.90e + 06	2
S02	021106	163808	35.2503	133.3815	7.4	1.29	4.52e + 05	3	1.90e + 06	2
S02	021107	164841	35.2558	133.3719	7.2	1.18	2.14e + 05	2	1.34e + 06	1
S02	021107	164841	35.2558	133.3719	7.2	1.18	2.14e + 05	2	1.34e + 06	1
S02	021225	060753	35.2608	133.3770	7.4	0.57	2.24e + 04	1	—	—
S02	021225	060753	35.2608	133.3770	7.4	0.57	2.24e + 04	1	—	—
S03	020827	034203	35.2272	133.3891	8.5	0.47	1.42e + 03	1	—	—
S03	020827	034203	35.2272	133.3891	8.5	0.47	1.42e + 03	1	—	—
S03	020920	170443	35.2327	133.3911	8.9	1.21	1.49e + 05	2	2.10e + 05	1
S03	020920	170443	35.2327	133.3911	8.9	1.21	1.49e + 05	2	2.10e + 05	1
S03	021024	194051	35.2313	133.3899	9.0	1.72	4.37e + 05	2	2.75e + 06	1
S03	021024	194051	35.2313	133.3899	9.0	1.72	4.37e + 05	2	2.75e + 06	1
S03	021107	201814	35.2359	133.3846	9.6	1.29	4.61e + 05	2	1.23e + 05	1
S03	021107	201814	35.2359	133.3846	9.6	1.29	4.61e + 05	2	1.23e + 05	1
S04	020329	014010	35.2143	133.4032	8.4	1.57	4.19e + 05	1	—	—
S04	020329	014010	35.2143	133.4032	8.4	1.57	4.19e + 05	1	—	—
S04	020627	112736	35.2219	133.4033	8.2	1.44	2.44e + 05	1	—	—
S04	020627	112736	35.2219	133.4033	8.2	1.44	2.44e + 05	1	—	—
S04	021105	022547	35.2144	133.4020	8.3	1.07	4.97e + 04	1	—	—
S04	021105	022547	35.2144	133.4020	8.3	1.07	4.97e + 04	1	—	—
S05	020922	095213	35.2219	133.4011	10.6	0.85	1.01e + 06	1	1.91e + 06	1
S05	020922	095213	35.2219	133.4011	10.6	0.85	1.01e + 06	1	1.91e + 06	1
S05	020926	063809	35.2117	133.4003	10.5	1.35	3.90e + 06	1	5.02e + 06	1
S05	020926	063809	35.2117	133.4003	10.5	1.35	3.90e + 06	1	5.02e + 06	1
S05	021020	070430	35.2164	133.3939	11.3	1.74	1.40e + 07	1	7.14e + 07	1
S05	021020	070430	35.2164	133.3939	11.3	1.74	1.40e + 07	1	7.14e + 07	1
S06	020610	063526	35.2143	133.4008	12.6	0.72	3.83e + 04	2	1.28e + 05	1
S06	020610	063526	35.2143	133.4008	12.6	0.72	3.83e + 04	2	1.28e + 05	1
S06	020910	112604	35.2138	133.4027	12.1	1.35	1.96e + 05	2	1.47e + 06	1
S06	020910	112604	35.2138	133.4027	12.1	1.35	1.96e + 05	2	1.47e + 06	1

†Number of stations used for E_s^P estimation. ‡Number of stations used for E_s^S estimation.

ported for micro earthquakes in South Africa gold mines that seismic energy changes before and after a relatively large event (e.g., Ogasawara *et al.*, 2002), though this has not been reported for natural tectonic earthquakes. It might also be possible that a transient change of average stress level in this area after the mainshock produced the size dependence of E_s/M_o or that the damage and cracks produced by the mainshock around the source region might facilitate earthquake occurrence with relatively lower stress drop. If this effect depends on earthquake size, it would result in a size dependence of E_s/M_o. It sounds rather ad-hoc, but unfortunately, the data set for this earthquake sequence is not sufficient to confirm or reject such hypothesis.

6. Conclusion

This is the first study that applied high-sampling data of Hi-net, Japanese nationwide high-sensitivity seismometer network, to study the scaling of seismic energy, E_s. In the discussion of scaling of E_s or E_s/M_o, a set of small size range of earthquakes can be misleading (e.g., Ide and Beroza, 2001). The 1k sps records contain signals at frequencies up to 200 Hz, which reduce the limit of event size down to about M_w 0.5. By comparing these events with the larger events including the mainshock, the difference of earthquake size in this study is about 9 orders of seismic moment.

Seismic energies E_s are determined using spectral ratios and an omega-square model assumption. The results are not easily understood. In the analysis of relatively large events with 100 sps data, E_s/M_o increases as M_o increases, with statistical significance. The analysis of smaller events with 1k sps data also suggests some size dependence. However, comparison of all events, including the mainshock, makes this trend ambiguous because there is an echelon-like structure segmented by each analysis band. A part of this trend might be an artifact due to limited bandwidth and/or inappropriate model assumptions, but we cannot rule out the possibility of temporal change in E_s/M_o scaling.

A shortcoming of this data set is that there are few events which can be analyzed by both 100 and 1k sps data because the start of 1k sps data delayed more than one year. However, as long as an event occurs within Japanese Islands, the same procedure is applicable and the following studies using future events should lead to more definitive conclusions.

Acknowledgments. We thank helpful comments from G. C. Beroza, A. Venkataraman, K. Imanishi, A. McGarr, E. Fukuyama and an anonymous reviewer. S. Ide is supported by Grant-in-Aid for Scientific Research and DaiDaiToku Project, Ministry of Education, Sports, Science and Technology, Japan.

References

Abercrombie, R. E., Earthquake source scaling relationships from ML −1 to 5 using seismograms recorded at 2.5-km depth, *J. Geophys. Res.*, **100**, 24,015–24,036, 1995.

Boatwright, J., Detailed spectral analysis of two small New York State earthquakes, *Bull. Seismol. Soc. Am.*, **68**, 1177–1131, 1978.

Boatwright, J. and G. L. Choy, Teleseismic estimates of the energy radiated by shallow earthquakes, *J. Geophys. Res.*, **91**, 2095–2112, 1986.

Brune, J. N., Tectonic stress and spectra of seismic shear waves from earthquakes, *J. Geophys. Res.*, **75**, 4997–5009, 1970.

Hough, S. E., Empirical Green's function analysis: Taking the next step, *J. Geophys. Res.*, **102**, 5369–5384, 1997.

Ide, S. and G. C. Beroza, Does apparent stress vary with earthquake size?, *Geophys. Res. Lett.*, **28**, 3349–3352, 2001.

Ide, S., G. C. Beroza, S. G. Prejean, and W. L. Ellsworth, Apparent break in earthquake scaling due to path and site effects on deep borehole, *J. Geophys. Res.*, **108**, 10.1029/2001JB001617, 2003.

Izutani, Y. and H. Kanamori, Scale-dependence of seismic energy-to-moment ratio for strike-slip earthquakes in Japan, *Geophys. Res. Lett.*, **28**, 4007–4010, 2001.

Kanamori, H., E. Hauksson, L. K. Hutton, and L. M. Jones, Determination of earthquake energy release and ML using TERRAscope, *Bull. Seismol. Soc. Am.*, **83**, 330–346, 1993.

Matsuzawa, T., M. Takeo, S. Ide, Y. Iio, H. Ito, K. Imanishi, and S. Horiuchi, S-wave energy estimation of small-earthquakes in the western Nagano region, Japan, *Geophys. Res. Lett.*, 2004 (in press).

McGarr, A., On relating apparent stress to the stress causing earthquake fault slip, *J. Geophys. Res.*, **104**, 3003–3011, 1999.

Obara, K., Hi-net: High sensitivity seismograph network, Japan, *Lecture Notes in Earth Sciences*, **98**, 79–87, 2002.

Ogasawara, H., S. Sato, S. Nishi, and H. Kawakata, the research group for semi-controlled earthquake generation experiments in South African deep gold mines, Temporal variation of seismic parameters associated with an Mw∼2 event monitored at a 100∼200 m distance, in *Seismogenic Process Monitoring*, edited by H. Ogasawara, T. Yanagidani, and M. Ando, pp. 173–184, 2002.

Prejean, S. G. and W. L. Ellsworth, Observations of earthquake source parameters and attenuation at 2 km depth in the Long Valley Caldera, Eastern California, *Bull. Seismol. Soc. Am.*, **91**, 165–177, 2001.

Waldhauser, F. and W. L. Ellsworth, A double-difference earthquake location algorithm: Method and application to the northern Hayward fault, California, *Bull. Seismol. Soc. Am.*, **90**, 1353–1368, 2000.

Wu, C., Estimation of fault geometry and slip-weakening parameters from waveform inversion and application to dynamic ruptures of earthquakes on a bending fault, Ph.D. thesis, University of Tokyo, 2004.

S. Ide (e-mail: ide@eps.s.u-tokyo.ac.jp), M. Matsubara (mk-matsu@bosai.go.jp), K. Obara (obara@bosai.go.jp)